Bio-Design and Manufacturing (2025) 8:994–1008
https://doi.org/10.1631/bdm.2500077

RESEARCH ARTICLE

In vivo 3D dose distribution verification for lung cancer: from rigid-body model to porcine lung

Yutao Zhang[1,2,3,4] · Kai Xie[1,2,3,4] · Lintao Song[1,2,3,4] · Jiewei Lai[5] · Haiping Zheng[6] · Qianjia Huang[7] · Hao Wang[7] · Tao Lin[1,2,3,4] · Liugang Gao[1,2,3,4] · Jiawei Sun[1,2,3,4] · Jianrong Dai[8] · Xinye Ni[1,2,3,4]

Received: 24 February 2025 / Accepted: 7 July 2025

Abstract

This study introduces a novel concept, biological in vivo three-dimensional (3D) dose distribution verification, aimed at investigating how respiratory motion affects the efficacy of lung cancer radiotherapy, representing an evolution from the current standard of rigid-body dose distribution verification. A 3D ex vivo biological lung motion simulation device (3D-BioLungEx) was designed to replicate human respiration. A radiotherapy plan of the patient was copied to the porcine lung, which was driven by 3D-BioLungEx to simulate various respiratory patterns that occur during treatment. To ensure anatomical consistency with the patient's lung structure, during transmission, skin, skeleton, and organs were adjusted according to CT images of the porcine lung. The patient's radiotherapy plan was then adapted to the porcine lung using the Monaco treatment planning system (TPS). Next, an iterative optimization and scatter inversion-based dose distribution retro-analysis algorithm (IOSI-BLDose) was developed to calculate the dose distribution during treatment. Gamma passing rates were used to quantify discrepancies between this dose distribution and that of the radiotherapy plan. When respiratory conditions were replicated, the passing rate reached up to 93.61%, while irregular breathing dropped it to 70%–90%, primarily due to amplitude changes. However, cycle variations had minimal impact. Compared to conventional rigid-body dose distribution verification, our method provides real-time biological feedback and more effectively captures motion-induced deviations. Accordingly, our biological in vivo 3D dose distribution verification has potential for improving treatment precision and enabling adaptive radiotherapy in clinical practice.

Yutao Zhang and Kai Xie have contributed equally to this work.

✉ Xinye Ni
nxy@njmu.edu.cn

[1] Department of Radiotherapy, The Second People's Hospital of Changzhou, The Third Affiliated Hospital of Nanjing Medical University, Changzhou 213003, China

[2] Jiangsu Province Engineering Research Center of Medical Physics, Changzhou 213003, China

[3] Center for Medical Physics, Nanjing Medical University, Changzhou 213003, China

[4] Changzhou Key Laboratory of Medical Physics, Changzhou 213003, China

[5] School of Biomedical Engineering and Informatics, Nanjing Medical University, Nanjing 211166, China

[6] Department of Research and Development, Guangzhou Raydose Medical Technology Co., Ltd., Guangzhou 510760, China

[7] School of Computer Science and Artificial Intelligence, Changzhou University, Changzhou 213159, China

[8] Department of Radiation Oncology, Cancer Hospital Chinese Academy of Medical Sciences, Beijing 100020, China

Graphical abstract

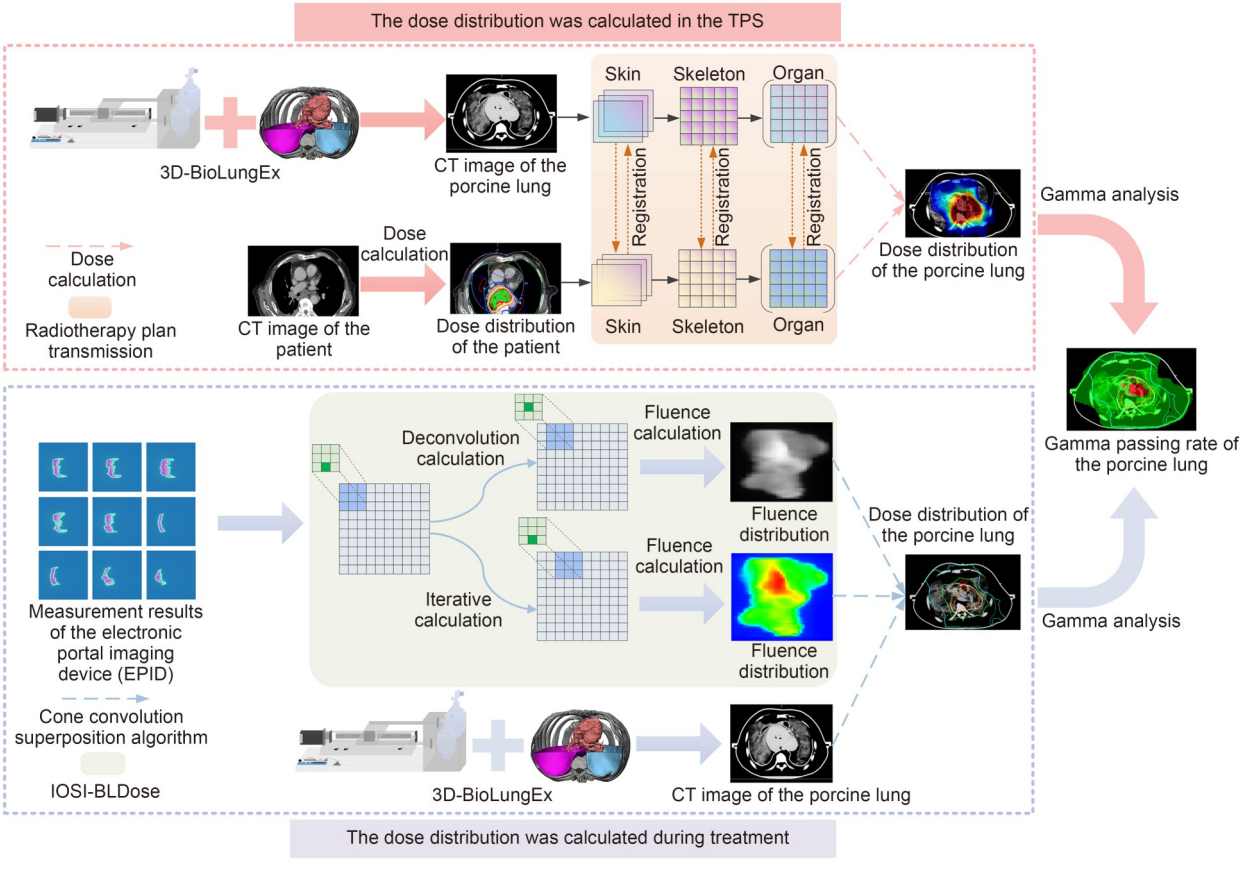

Keywords Biological lung · 3D printing · Motion simulation device · Radiotherapy · Lung cancer · Dose distribution verification

1 Introduction

Lung cancer is the leading cause of cancer-related mortality, with an estimated 1.8 million deaths, accounting for 18.7% of all global cancer deaths in 2022 [1]. Radiotherapy plays a crucial role in the treatment of lung cancer. Evidence-based modeling indicates that 77% of lung cancer patients will require radiotherapy at some point during their cancer treatment [2].

In lung cancer radiotherapy, dose distribution is traditionally calculated based on a specific static phase of the patient's respiratory cycle captured during computed tomography (CT) simulation [3]. However, the tumor position in lung cancer patients changes due to respiratory motion and other physiological movements. To address this issue, the American Association of Physicists in Medicine (AAPM) recommends the use of respiratory motion simulation devices to verify the dose distribution before the first treatment, ensuring the accuracy of the radiotherapy treatment [4].

Classic respiratory simulation models, such as the ADAM model [5], the Laerdal Medical cardiopulmonary resuscitation (CPR) training manikin [6], and the ARDOS model [7], are primarily mechanical. These models replicate respiratory motion using motor-driven systems but lack anatomical fidelity, limiting their ability to accurately simulate human respiratory structures. In contrast, Perrin et al. [8] developed the LuCa anthropomorphic thoracic respiratory model, which incorporates inflatable lung tissue and realistic skeletal and muscular components. This model provides external realism and replicates the surface motion associated with tumor movement, but struggles with replicating lung tissue elasticity and complex deformations.

Thus, although mechanical models can simulate some physical aspects of respiratory motion, they fail to capture the full complexity of biological tissues. To address this issue, researchers have turned to ex vivo lung tissue models cultured under near-physiological conditions. For example,

Bondesson et al. [9], Rabe et al. [10], and Albers et al. [11] employed vacuum pump systems to control lung expansion and contraction, while Mann et al. [12] simulated diaphragmatic motion using a silicone balloon beneath a porcine lung. Despite their improved biological realism, these models still struggle to simulate diverse respiratory conditions and match individual patient characteristics, leading to discrepancies with clinical outcomes.

In addition, most mechanical and biological models focus on theoretical tumor motion studies and do not address in vivo dose distribution verification during treatment. For radiotherapy, in vivo dose verification refers to anatomically realistic dose evaluation setups and does not necessarily imply the use of living tissues or subjects. Current dose distribution verification systems are either two-dimensional (2D) or three-dimensional (3D). Representative 2D devices include Matrixx (IBA, Leuven, Belgium) [13] and MapCHECK (Sun Nuclear, Melbourne, Florida, USA) [14], while 3D systems include Compass (IBA) [15], Octavius (PTW, Freiburg, Germany) [16], ArcCHECK (Sun Nuclear) [17], and Delta4 (ScandiDos, Uppsala, Sweden) [18]. All rely on rigid-body models, and some incorporate motion platforms to simulate relative movement. However, the detector or film layer remains fixed, resulting in rigid-body motions that cannot accurately replicate the dynamic behavior of biological tissues, particularly respiration-induced motion. Additionally, these devices are used prior to treatment to verify the alignment between the linear accelerator output and the treatment plan, but cannot account for the real-time impact of respiratory motion on dose distribution during treatment.

To overcome these limitations, an ideal dose distribution verification device should integrate the following features: (1) a system capable of realistically simulating patient-specific respiratory motion patterns with biomimetic fidelity, allowing high-resolution radiographic imaging under real-time conditions, as well as portability and appropriate sizing; (2) a robust algorithm capable of reliably measuring 3D radiation dose distribution, enabling precise measurements and ensuring accuracy. Such a device would be critical for simulating and optimizing the entire adaptive radiotherapy workflow, from CT simulation and treatment planning to dose delivery and verification.

To address these challenges, we propose an innovative method for biological in vivo 3D dose distribution verification. The main contributions of this work are as follows:

1. Development of a 3D dynamic biological ex vivo lung respiratory simulation device (3D-BioLungEx): This device integrates advanced automation technology, being highly customizable to replicate patient-specific respiratory patterns. By driving a biological lung to simulate human respiration, it achieves physiological realism in the verification environment. Fresh porcine lungs, structurally similar to human lungs, were adopted as a lung model. Specifically, both porcine and human lungs have two lobes on the left and three on the right, with comparable bronchial tree branching, airway diameter, and tissue elasticity. In addition, using preoperative CT imaging data and high-precision 3D printing, we constructed a thoracic cavity model to house the porcine lung, enhancing anatomical accuracy in the simulated environment.

2. Design of the IOSI-BLDose algorithm: An iterative optimization and scatter inversion-based dose distribution retro-analysis algorithm (IOSI-BLDose) for biological lungs was developed to calculate dose distributions within the porcine lung. Employing the gamma algorithm with a 3%/3 mm dose−distance criterion, discrepancies between the calculated dose distribution and the radiotherapy treatment plan were quantified, offering insights into gamma passing rates [19].

2 Methods

2.1 3D-BioLungEx

The 3D-BioLungEx was first developed in this study to facilitate real-time monitoring and precise simulation of respiratory patterns in lung cancer patients. This device comprises three modules: a monitoring module, a phantom module, and an actuator module. The first employs laser ranging technology for non-contact measurement of the patient's respiratory curve, achieving an error margin <3 mm. The second is designed to create a customized thoracic cavity for the patient using 3D-printing technology. The third replicates the patient's respiratory motions using a stepper motor.

2.1.1 Monitoring module

Figure 1a presents a schematic of the monitoring module in the 3D-BioLungEx. The laser rangefinder projects onto the patient's chest area. The real-time distance (d) between the patient's chest surface and the laser emitter can be defined as follows [20]:

$$d = \frac{c_0(t_2 - t_1)}{2}, \tag{1}$$

where c_0 represents the speed of light (c_0=299 792.458 km/s), t_1 denotes the time for the laser pulse to reach the chest surface, and t_2 indicates the time for the pulse to return to the rangefinder after reflecting off the surface.

The laser rangefinder continuously emitted light pulses to measure the distance (d) in real time, storing this information in an STM32 microcontroller. The laser rangefinder used in the monitoring module operated at an acquisition frequency of 10 Hz, sufficient to accurately capture the respiratory waveform in real time. The microcontroller automatically identified the end exhalation position (d_1) and the end inhalation position (d_2) during each respiratory cycle. The difference between d_2 and d_1 represents the amplitude of the

respiratory curve [21]. Additionally, a pressure sensor attached to the chest area captured signal fluctuations, which were displayed on a monitor to record the respiratory cycle. Figure 1b provides a detailed view of the components of the monitoring module. Figure 1c illustrates the clinical application setting for the monitoring module, where a Brilliance Big Bore CT scanner (ROYAL PHILIPS, Amsterdam, the Netherlands) was used to capture four-dimensional (4D) CT images of lung cancer patients. These images are critical for accurate respiratory simulation and treatment planning.

2.1.2 Phantom module

In this study, to evaluate the performance of our proposed 3D-BioLungEx system in dose verification, ArcCHECK (Sun Nuclear) was selected as a comparator. ArcCHECK is a widely used 3D dose verification device in radiotherapy, being fundamentally a static system. During verification, the linear accelerator delivers the treatment beam to the ArcCHECK cylindrical phantom, which contains an array of diode detectors in a spiral pattern. These detectors capture the dose distribution and allow for gamma index analysis to evaluate the accuracy of the radiation delivery. However, ArcCHECK does not account for respiratory-induced organ motion, something particularly critical in thoracic tumors such as lung cancer. Furthermore, ArcCHECK is designed as a general-purpose quality assurance tool applicable across a wide range of anatomical sites, lacking the anatomical specificity and motion adaptability required for patient-specific verification in lung cancer treatment.

To overcome these limitations, we developed a customized phantom module in the 3D-BioLungEx system, enabling individualized modeling of thoracic motion and anatomy. Figure 2 shows a schematic of the phantom module in the 3D-BioLungEx. Based on the patients' 4D CT images, a unique, custom thoracic cavity was created for each using computer-aided design (CAD) technology. The process comprised the following steps (Fig. 2):

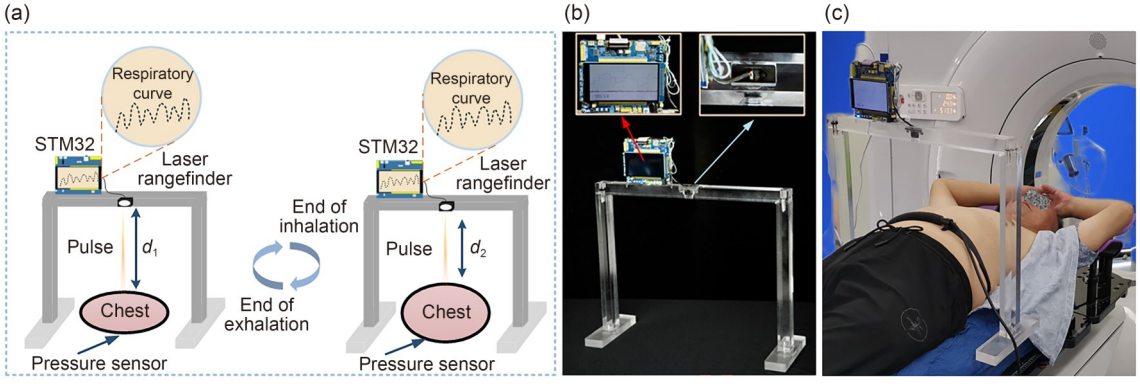

Fig. 1 Overview of the monitoring module in the 3D-BioLungEx. (a) Schematic of the monitoring module structure of the 3D-BioLungEx, illustrating the collection of respiratory signal data throughout a complete respiratory cycle in the patient. (b) Photograph of the monitoring module of the 3D-BioLungEx, including an STM32 microcontroller, a laser rangefinder, and a supporting structure made from acrylic plates. (c) An actual patient where the monitoring module was used to scan 4D CT

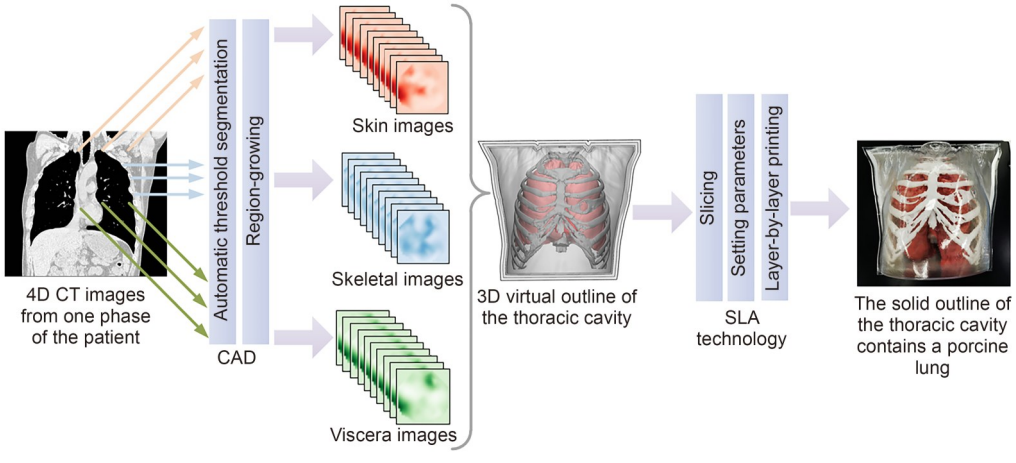

Fig. 2 Overview of the phantom module in the 3D-BioLungEx. Threshold segmentation and region-growing techniques were applied to the patient's CT images to extract 3D models of key tissues. Once the design was complete, these virtual models were converted into solid models using a stereolithography apparatus (SLA)

First, 4D CT images of the patient's chest were acquired using a Brilliance Big Bore CT scanner (ROYAL PHILIPS). Scanning parameters were a slice thickness of 1 mm and a matrix size of 512×512. After the scan, the acquired data were reconstructed at the same 1-mm slice thickness to produce lung window 4D CT images [22], which were then imported into medical image-processing software (version 1.0; Jinse Medical Information Technology Co., Ltd., Changzhou, China). Using automatic threshold segmentation and region-growing techniques, 3D models of critical structures such as skin, bones, heart, and lungs were independently extracted [23].

After designing the model, a photosensitive resin (Union Tech, Shanghai, China) was chosen and cast into a model reservoir. The liquid resin was cured under ultraviolet (UV) light at a wavelength range of 250 to 400 nm [24]. Upon UV exposure, the resin was rapidly cured, forming a solidified layer within 0.05–0.10 s. A stereolithography apparatus (SLA) was then used to build the 3D model by layering these cured resin sheets [25]. Then, the SLA component was cleaned to eliminate any residual uncured resin from its surface. After cleaning, the model was subjected to final curing in a UV oven, yielding a complete and anatomically accurate 3D solid entity.

2.1.3 Actuator module

Vacuum pump systems are among the most widely used devices for generating inflation–deflation cycles in ex vivo lung ventilation studies, due to their simplicity, accessibility, and ability to mimic negative pressure-driven breathing. In this study, a vacuum pump (NRL180A, ULVAC, Ningbo, China) (https://www.ulvac.com.cn/product/product.php?id=399) was used to ventilate excised porcine lungs. The device was connected to the trachea via an airtight flexible hose, applying intermittent negative pressure to induce inflation and allowing passive deflation upon release.

Despite these advantages, conventional vacuum pump systems offer limited flexibility in simulating patient-specific respiratory patterns and do not allow real-time monitoring or individualized control. To address these limitations, we independently developed an actuator module to facilitate real-time monitoring and precise replication of respiratory dynamics in lung cancer patients.

Figure 3a provides a schematic of the actuator module in the 3D-BioLungEx, which has three core functions: control, drive, and compression. First, the respiratory curves recorded by the monitoring module were imported into the actuator module, which incorporates a control board equipped with a high-performance ATmega328P-PU chip. This board conducted calculations and generated pulse signals via an internal picopower 8-bit AVR microcontroller. Then, the generated pulse signals were transmitted into a stepper motor connected with the lead screw at its output end. As the stepper motor rotated, it drove the lead screw's movement, which in turn moved a slider along its length. A U-shaped fork attached to the slider advanced or retracted with the lead screw's rotation [26], while the pulse signal's frequency and quantity precisely controlled the rotation distance and speed of the stepper motor [27].

To align with the amplitude of the patient's respiratory curve, parameters in the "for loop" function in Arduino-1.8.19 were adjusted to control the number of forward and reverse rotations of the stepper motor, thereby modulating the air volume in the storage balloon. Each complete motor rotation resulted in a linear change in balloon volume (i.e., a fixed advance or retraction distance). The elastic properties of the porcine lung were approximated using a linear spring model [28, 29]. Airflow resistance was considered proportional to the pressure differential and flow rate [30, 31], while

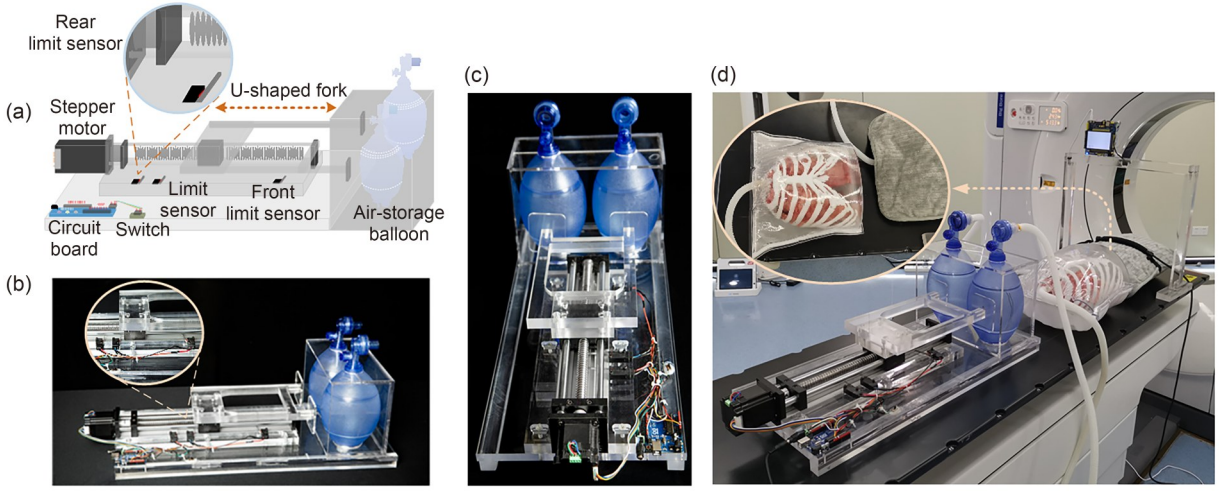

Fig. 3 Overview of the actuator module in the 3D-BioLungEx. (a) Schematic of the actuator module structure. (b) Side view photograph. (c) Top view photograph. (d) Real acquisition of 4D CT images

environmental factors such as temperature and humidity were neglected due to their minimal impact on gas properties. The relationship between motor rotation and lung respiratory amplitude (A) can be defined as follows:

$$A \approx \frac{k_{\text{elastic}}^{-1}\beta\left(V_{\text{balloon}} - V_{\min}\right)}{V_{\text{lung}}} = \frac{k_{\text{elastic}}^{-1}\beta NL}{V_{\text{lung}}}, \quad (2)$$

where k_{elastic} denotes the elasticity coefficient of the porcine lung, β is a proportional coefficient, V_{balloon} represents the balloon volume, $V_{\min}$ is the lung volume at full expiration, V_{lung} is the maximum lung volume, N denotes the number of motor rotations, and L represents the displacement of the air-storage balloon per motor rotation.

Additionally, modifying the delay function parameters controlled the transition time between forward and reverse rotations, aligning with the subject's respiratory pauses. To ensure simulation accuracy, a front limit sensor and a rear limit sensor were strategically positioned along the lead screw's path [32]. These sensors effectively constrained the range of motion of the U-shaped fork based on predefined distance parameters. The power source provided energy to the entire device.

2.2 IOSI-BLDose

2.2.1 Calculation of flux distribution after lung transmission

The high-energy X-rays emitted from the radiation source penetrated the porcine lung, interacting with lung tissue. When moving from the source into the air or a medium, they spread and create a scattered field that describes the spatial intensity and distribution of the X-rays [33]. An electronic portal imaging device (EPID) was positioned beneath the porcine lung to detect photons scattered from within the tissue, forming a characteristic 2D intensity distribution pattern on the EPID surface that reflects the spatial variation of scattered radiation emerging from different depths and locations within the lung tissue. This spatially resolved scatter distribution, termed "EPID surface flux," provides quantitative information about the tissue's heterogeneous scattering properties and photon interaction patterns [34]. The EPID's detected signal included the scattered photons and the primary radiation beam, requiring deconvolution to separate them into the flux distribution after transmission through the porcine lung tissue [35].

2.2.2 Calculation of flux distribution before lung transmission

Ray tracing can reconstruct the exact path followed by X-rays from the source through the porcine lung tissue [36]. As shown in Fig. 4a, $\boldsymbol{P}_0$ represents the initial flux distribution before the X-rays enter the porcine lung. The flux at point x in $\boldsymbol{P}_0$ can be expressed as follows:

$$D(x) = \int T(s)K(s-x)\mathrm{d}V, \quad (3)$$

where $T(s)$ represents the total energy released per unit mass. The term $K(s–x)$ is the flux distribution kernel function from s to x, describing the distribution of flux created in water after photon interaction.

2.2.3 Retroactive calculation of dose distribution within the porcine lung

When X-rays enter the porcine lung, they initially undergo scattering, as described by $\boldsymbol{P}_0$ and $\boldsymbol{P}_1$ (scattering factors). During this phase, the lung tissue generates secondary scattered rays, which get attenuated by both scattering and absorption losses, represented by $\boldsymbol{P}_0'$ and $\boldsymbol{P}_1'$ (attenuated scattering rates and factors, respectively). As X-rays undergo

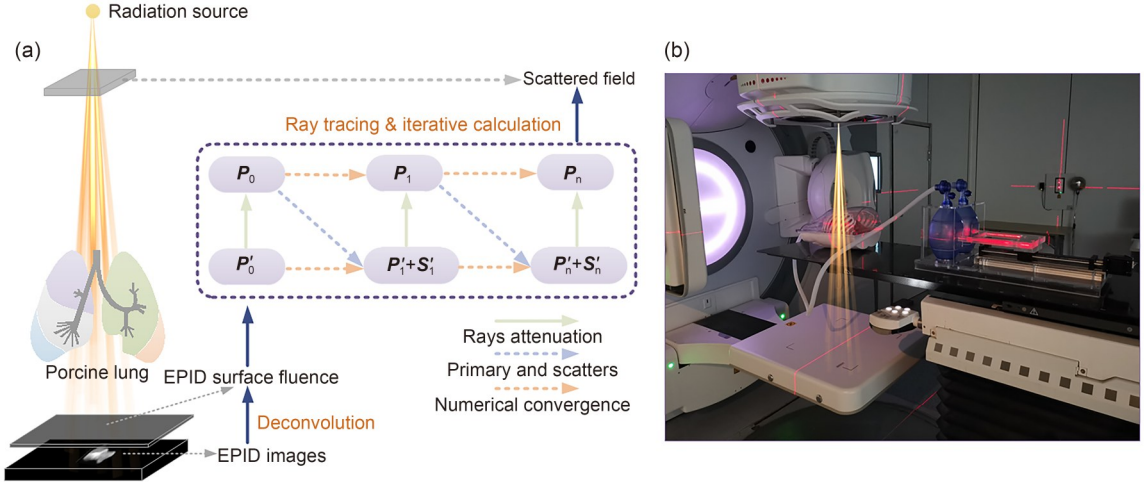

Fig. 4 Overview of IOSI-BLDose. (a) Schematic illustrating the dose distribution calculation in the porcine lung using IOSI-BLDose. (b) Photograph showing a clinical application scenario for 3D-BioLungEx and IOSI-BLDose

multiple scattering and absorption events while traversing the porcine lung, iterative calculations were required to accurately model these processes [37]. This iterative approach incorporated the effects of varying tissue densities, thicknesses, and scattering characteristics on the radiation beam. In each iteration, the flux distribution of the radiation source was adjusted based on the current dose distribution and scattering properties. The iterative optimization process was as follows: $\boldsymbol{P}_0$ entered the CCCS algorithm engine [38], which considered scattering and absorption effects to calculate the total dose distribution, $\boldsymbol{P}_1'+\boldsymbol{S}_1'$, including the scattering contribution. $\boldsymbol{S}_1'$ represents the attenuated absorption factors. The calculated $\boldsymbol{P}_1'+\boldsymbol{S}_1'$ was compared with $\boldsymbol{P}_0'$. Any discrepancy between them indicated that the initial $\boldsymbol{P}_0$ was inaccurate, necessitating an iterative adjustment of $\boldsymbol{P}_0$ until the difference fell below a predefined threshold. Achieving this threshold signified convergence. After several iterations, the optimized flux distribution $\boldsymbol{P}_\mathrm{n}$ was obtained, with $\boldsymbol{P}_\mathrm{n}(\boldsymbol{P}_\mathrm{n}'+\boldsymbol{S}_\mathrm{n}')$ representing the dose distribution within the porcine lung. $\boldsymbol{S}_\mathrm{n}'$ represents the optimal attenuated absorption factors after multiple iterative calculations. A brief clinical demonstration of 3D-BioLungEx and IOSI-BLDose is shown in Fig. 4b.

3 Results

3.1 Dataset

A total of 50 lung cancer patients from the Second People's Hospital of Changzhou (from July 2024 to December 2024) were enrolled, including 27 males and 23 females, with a mean age of (59.82±8.62) years. The control group comprised 30 healthy individuals, matched in sex, age, and education, with a mean age of (57.26±7.81) years. No significant differences were observed between the two groups ($p>0.05$). Respiratory curves were recorded in a CT simulation room using the 3D-BioLungEx monitoring module. For the patient group, normal respiratory curves were recorded during positioning. The control group simulated three abnormal respiratory patterns—Cheyne–Stokes (CS) breathing, yawning, and coughing—without CT scanning to minimize radiation exposure.

3.2 3D-BioLungEx simulation of respiratory curves

Figure 5a illustrates the respiratory curve of a randomly selected patient in the CT simulation room, captured in real time from the monitoring screen. Figure 5b presents the simulation of this respiratory curve generated by 3D-BioLungEx, called the CT-sim curve. This simulated curve closely mirrors the actual respiratory curve shown in Fig. 5a, effectively replicating the periodic fluctuations and amplitude characteristics of the patient's breathing. Figures 5d, 5g, and 5j illustrate respiratory curves for CS breathing, yawning, and coughing, respectively, while Figs. 5e, 5h, and 5k display the simulated outputs of 3D-BioLungEx for these three abnormal respiratory patterns.

To further quantify the simulation accuracy of 3D-BioLungEx, a unified Cartesian coordinate system was established, as shown in Figs. 5c, 5f, 5i, and 5l. Within this coordinate system, the actual respiratory curves recorded during monitoring were overlaid with the simulated ones for comparison.

3D-BioLungEx demonstrated superior respiratory simulation accuracy compared to the vacuum pump across all tested breathing patterns, with significantly lower error rates in both normal and abnormal respiratory conditions (Table 1). In normal respiratory curves from 50 lung cancer patients undergoing CT simulation positioning, 3D-BioLungEx achieved substantially better performance across all metrics (mean absolute error (MAE): (0.81±0.08) mm vs. (2.06±0.89) mm; root mean square error (RMSE): (0.98±0.12) mm vs. (1.53±0.74) mm; mean absolute percentage error (MAPE): (8.94±1.77)% vs. (27.01±8.08)%, $p<0.05$), demonstrating superior accuracy due to its precise control over amplitude and cycle.

The performance advantage of 3D-BioLungEx was even more pronounced in abnormal respiratory patterns simulated by 30 healthy volunteers. For CS breathing, 3D-BioLungEx showed significantly lower errors (MAPE: (6.87±1.43)% vs. (24.59±7.07)%, $p<0.05$), accurately replicating the characteristic pauses while the vacuum pump struggled with these nuances. In yawning simulations, despite minor discrepancies at the end of the inhalation phase, 3D-BioLungEx maintained superior accuracy (MAPE: (16.94±8.12)% vs. (26.94±8.12)%, $p<0.05$). When simulating coughing, the most challenging condition due to its dynamic nature, 3D-BioLungEx still achieved reasonable accuracy (MAPE: (19.45±9.19)% vs. (39.45±12.19)%, $p<0.05$), whereas the vacuum pump struggled with the complex dynamics, producing significantly more errors across all metrics.

Overall, 3D-BioLungEx demonstrated superior performance across all respiratory patterns, offering precise and flexible simulations. Its advanced control mechanisms make it particularly effective for applications in radiotherapy, where accurate respiratory motion modeling is crucial. In contrast, the limitations of the vacuum pump in simulating complex respiratory features were evident in all tested scenarios.

3.3 Qualitative comparison of dose distributions

Figure 6 presents multi-angle views from lung CT scans, comparing the patient, 3D-BioLungEx, and ArcCHECK in the axial, coronal, and sagittal planes. The first rows of

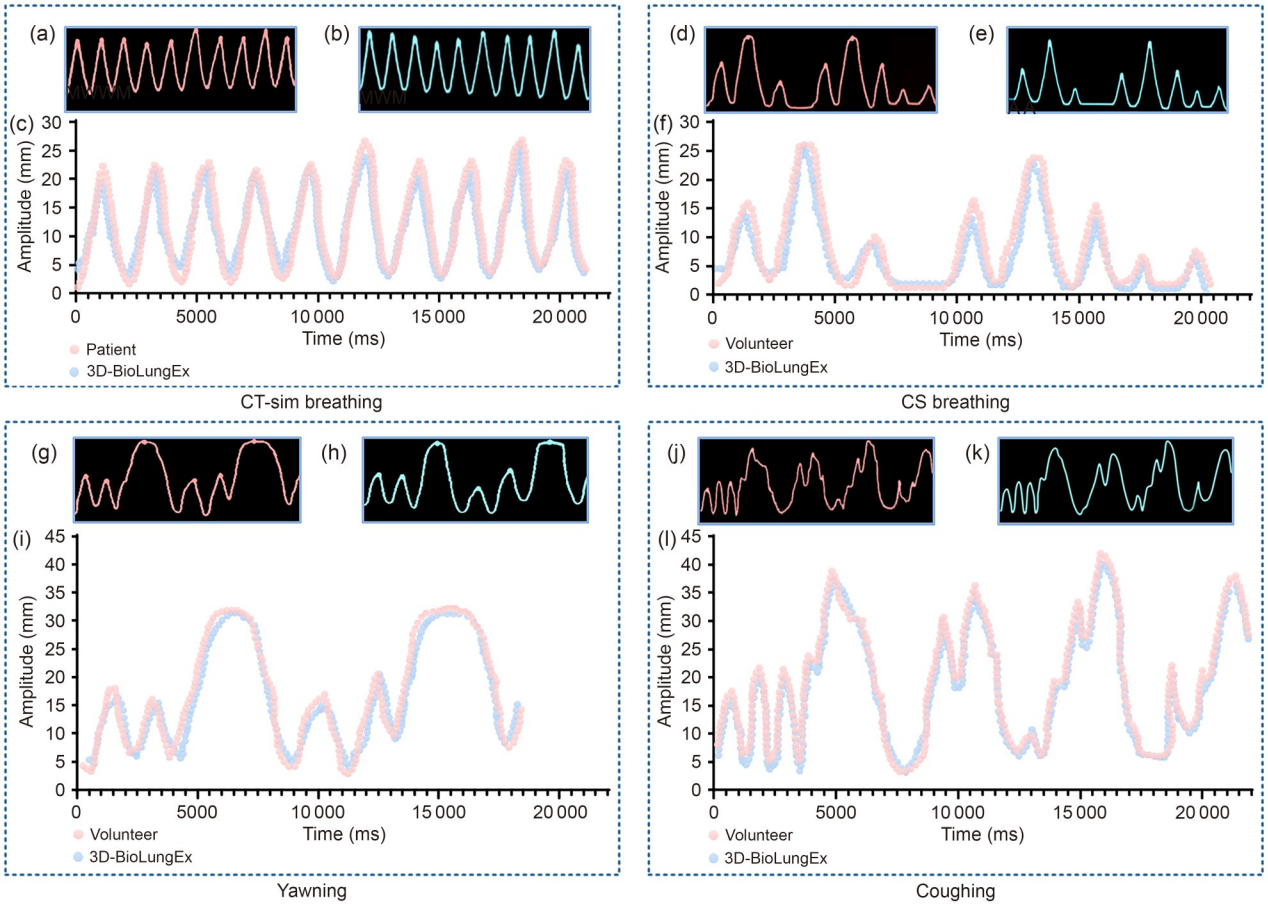

Fig. 5 Respiratory curve charts. (a) Normal respiratory curve measured in the CT simulation room. (b) Normal respiratory curve simulated by 3D-BioLungEx. (c) Comparison of normal respiratory curves. (d) CS respiratory curve simulated by a volunteer. (e) CS respiratory curve simulated by 3D-BioLungEx. (f) Comparison of CS respiratory curves. (g) Yawning respiratory curve simulated by a volunteer. (h) Yawning respiratory curve simulated by 3D-BioLungEx. (i) Comparison of yawning respiratory curves. (j) Coughing respiratory curve simulated by a volunteer. (k) Coughing respiratory curve simulated by 3D-BioLungEx. (l) Comparison of coughing respiratory curves

Table 1 Accuracy of 3D-BioLungEx and vacuum pump in simulating respiratory curves across different respiratory patterns

Device	Pattern	Curve	MAE (mm)	RMSE (mm)	MAPE (%)
3D-BioLungEx	Normal (n=50)	CT-sim breathing	0.81±0.08	0.98±0.12	8.94±1.77
	Abnormal (n=30)	CS breathing	0.56±0.15	0.79±0.28	6.87±1.43
	Abnormal (n=30)	Yawning	1.21±0.70	1.81±0.94	16.94±8.12
	Abnormal (n=30)	Coughing	1.92±0.98	2.33±1.06	19.45±9.19
Vacuum pump	Normal (n=50)	CT-sim breathing	2.06±0.89*	1.53±0.74*	27.01±8.08*
	Abnormal (n=30)	CS breathing	1.97±0.58*	1.01±0.45*	24.59±7.07*
	Abnormal (n=30)	Yawning	2.85±1.04*	1.95±0.70*	26.94±8.12*
	Abnormal (n=30)	Coughing	3.97±1.72*	2.62±1.28*	39.45±12.19*

Values are expressed as mean±standard deviation. Two-sided p value from one-way analysis of variance (ANOVA) with Bonferroni post hoc analysis; *p<0.05 vs. 3D-BioLungEx in the same curve

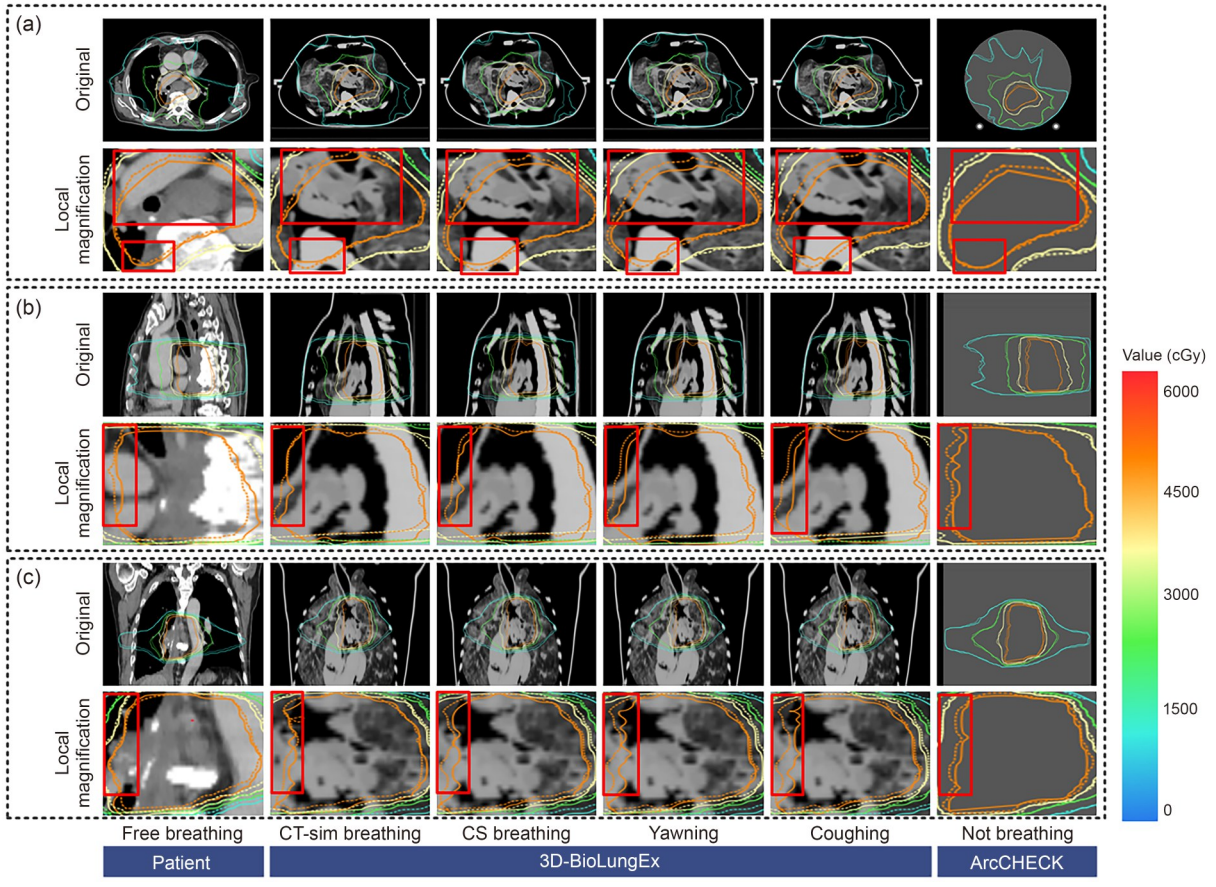

Fig. 6 Qualitative comparison of biological in vivo 3D dose distribution. (a) Dose distributions in the axial CT (the first row, original CT images; the second row, magnified views of high-dose regions, with red boxes highlighting areas exhibiting significant differences between planned and measured dose distributions). (b) Dose distributions in the coronal CT (the first row, original CT images; the second row, magnified views of high-dose regions, with red boxes highlighting areas exhibiting significant differences between planned and measured dose distributions). (c) Dose distributions in the sagittal CT (the first row, original CT images; the second row, magnified views of high-dose regions, with red boxes highlighting areas exhibiting significant differences between planned and measured dose distributions)

Figs. 6a, 6b, and 6c provide a clear comparison between the planned dose distribution (solid lines) and the measured dose distribution (dashed lines) in the 3D space. Solid lines represent the dose distribution planned for the patient using the Monaco treatment planning system (TPS, version 5.40.02; Elekta Instrument AB, Stockholm, Sweden), which optimizes the radiation dose based on the tumor's location and the surrounding healthy tissue. Dashed lines represent the dose distribution as delivered during treatment, providing a real-time comparison of the treatment's accuracy. The dose distributions in Fig. 6 are color-coded to represent different dose levels, with the corresponding scale on the right. Green dose lines indicate an approximate dose of 1500 cGy, yellow lines represent 3000 cGy, and red lines represent up to 6000 cGy.

The second-row images of Figs. 6a, 6b, and 6c, magnified and highlighted with red boxes, are extracted from regions of high-dose distributions. These areas are critical for assessing the precise spatial alignment between the planned and delivered doses. By magnifying these regions, we can more effectively observe discrepancies in dose delivery, especially in high-dose regions where even small errors can have a significant clinical impact. In particular, these images help illustrate spatial discrepancies between planned and delivered doses, such as potential shifts in the dose profile or any inconsistencies in the dose gradient.

For image comparisons, CT scans of the ArcCHECK phantom were acquired and co-registered with the patient's and 3D-BioLungEx CT data. Compared with 3D-BioLungEx, CT images of ArcCHECK exhibited significant deviations from the patient's CT images, lacking biological tissue structures. This lack of detail rendered the visualization of the lung's complex anatomical structure difficult. Conversely, 3D-BioLungEx had high fidelity; its CT images closely resembled those of the patient, featuring realistic biological tissues and a 3D-printed thoracic cavity.

In terms of dose distribution, we observed discrepancies between the planned and measured 3D dose lines in the patient under free-breathing conditions, highlighting the substantial impact of natural respiratory motion on dose delivery

accuracy. In addition, 3D-BioLungEx simulating regular, controlled breathing in a CT simulation setting showed noticeably smaller deviations due to more consistent motion patterns. When simulating three types of irregular breathing patterns (CS breathing, yawning, and coughing) during treatment, 3D-BioLungEx showed higher mismatch with increasing respiratory irregularities, most notably in the coughing scenario.

ArcCHECK measurements were performed under static, non-breathing conditions as a baseline reference. However, due to the absence of biological tissue structures, ArcCHECK failed to capture the complex anatomical changes induced by respiratory motion. In contrast, 3D-BioLungEx had high fidelity in replicating patient-specific respiratory patterns and thoracic anatomy.

3.4 Quantitative validation results of in vivo 3D dose distribution

Figure 7 illustrates the dose passing rates for the patient, 3D-BioLungEx, and ArcCHECK during treatment. Green areas indicate regions where the dose passed, whereas red areas mark regions where the dose did not pass. The first column visually presented the dose passing rate for the patient undergoing treatment in free-breathing mode, achieving a gamma passing rate of 91.22%. The second column shows the dose passing rate for 3D-BioLungEx simulating the patient in the CT simulation room under normal breathing conditions, with a smaller red area than that in the first column, demonstrating an improved passing rate of 93.47%. The third to fifth columns display the dose passing rates for 3D-BioLungEx simulating the patient under three common abnormal breathing patterns during treatment, with CS breathing showing 85.38%, yawning pattern achieving 82.63%, and coughing resulting in the lowest passing rate of 78.54%. These columns clearly illustrate the impact of these non-standard breathing patterns on dose distribution, with passing rates decreasing progressively as breathing patterns become more irregular, aiding in evaluating the robustness of the radiotherapy plan. The final column presents the dose-validation results of ArcCHECK under static, non-breathing conditions as a control, achieving the highest passing rate of 95.86%. The smallest red area highlighted the significant impact of respiratory motion on dose distribution. The trend of red area changes across columns indicated that with variations in breathing patterns, the regions of dose failure increased, particularly under abnormal breathing patterns, with a 17.32% difference between the best static condition (95.86%) and the worst breathing pattern (78.54%). Conversely, the dose passing rate was optimal under the static, non-breathing condition.

Figure 8 provides a comprehensive comparative analysis of dose distribution characteristics along the *X*- and *Y*-axis, derived from mark points placed on the patient's body. Mark points serve as crucial reference points for establishing a unified coordinate system on the patient's anatomy. They enable direct comparison between TPS preset doses and actual measured doses, revealing differences and uncertainties during treatment. Note that Fig. 8a specifically describes dose distributions in the axial plane, while Figs. 8b and 8c do it for the coronal and sagittal planes, respectively. This distinction is crucial for understanding the spatial orientation of the dose distributions and their variations across anatomical planes.

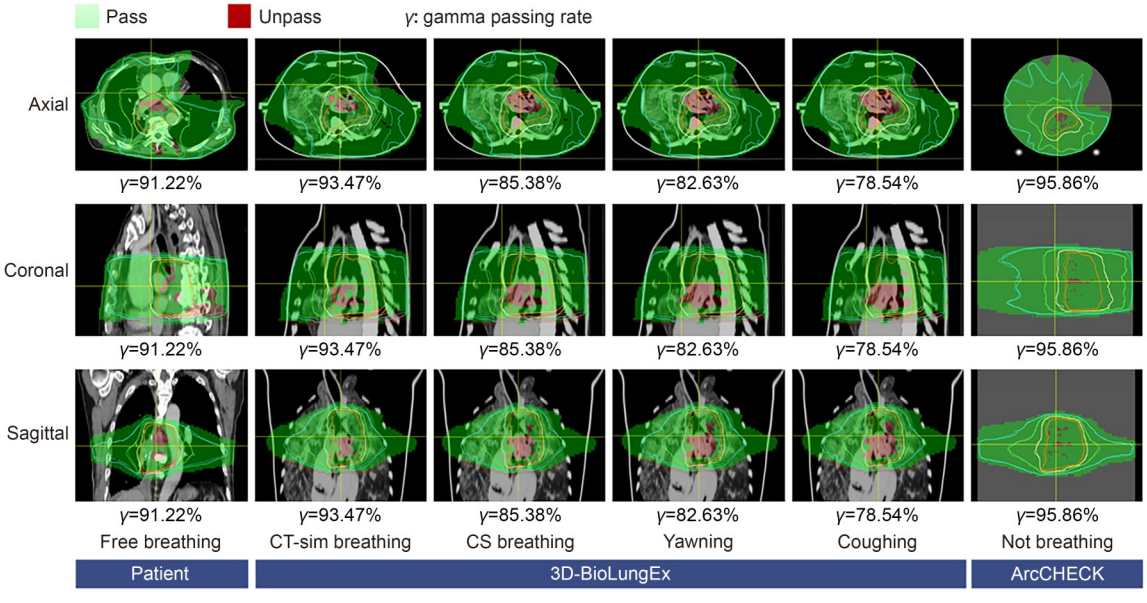

Fig. 7 Quantitative verification of biological in vivo 3D dose distribution. Comparison of dose passing rates among the patient, 3D-BioLungEx, and ArcCHECK. Green areas indicate passing regions, whereas red areas mark non-passing regions

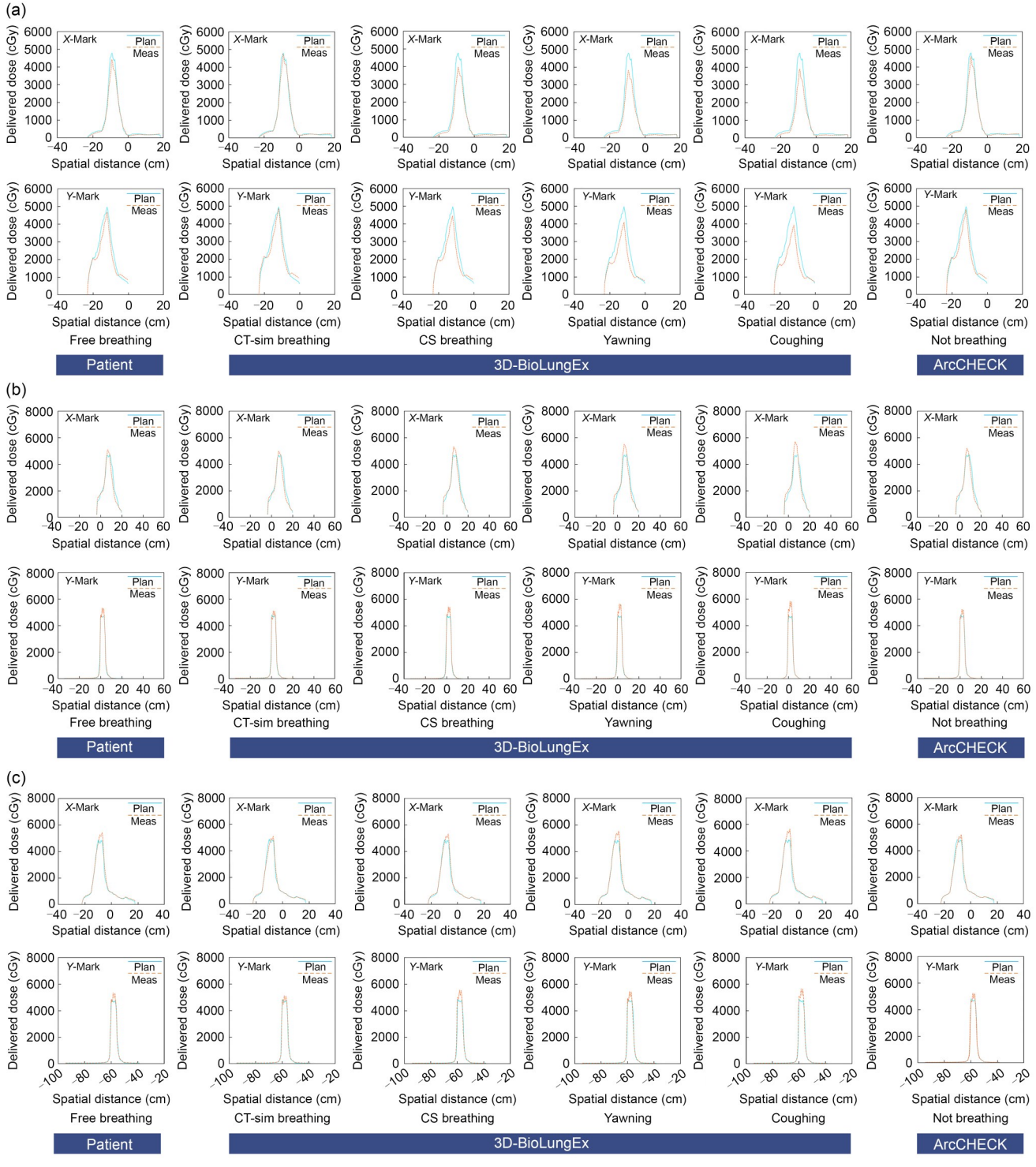

Fig. 8 Dose distributions at marker points. (a) Comparative dose distributions in the axial CT along the *X*- and *Y*-axis for the patient, 3D-BioLungEx, and ArcCHECK. (b) Comparative dose distributions in the coronal CT along the *X*- and *Y*-axis for the patient, 3D-BioLungEx, and ArcCHECK. (c) Comparative dose distributions in the sagittal CT along the *X*- and *Y*-axis for the patient, 3D-BioLungEx, and ArcCHECK

Blue solid lines represent the planned dose distributions preset by the TPS, while brown dashed lines indicate the measured dose distributions calculated during treatment. Under free-breathing conditions, there were discrepancies between the TPS preset dose distribution and the actual measured dose distribution along both axes. These discrepancies are most pronounced in dose peak regions, highlighting the complexity and inherent uncertainties of the treatment process.

Figure 9 presents experimental results on global and local gamma passing rates with varying respiratory patterns.

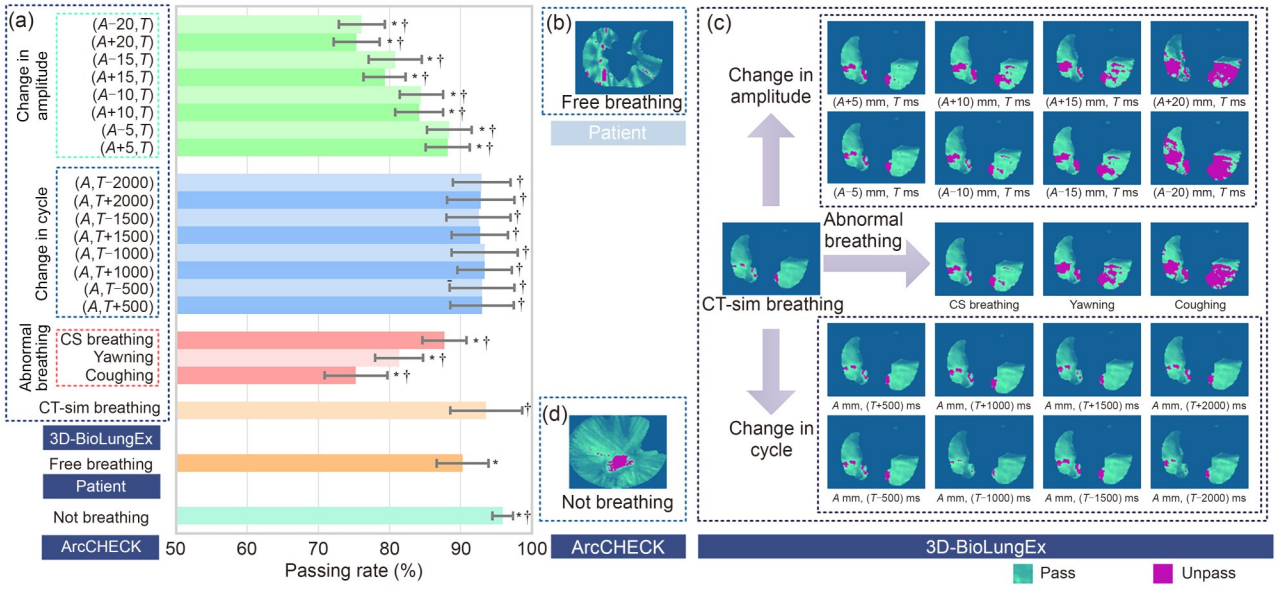

Fig. 9 Global and local gamma passing rates under different respiratory patterns. (a) Bar graph representation of global gamma passing rates for 3D-BioLungEx, patient, and ArcCHECK. Values are expressed as mean±standard deviation, n=50 for each group. Two-sided p value was calculated from one-way analysis of variance (ANOVA) with Bonferroni post hoc analysis. $^{*}p<0.05$ vs. 3D-BioLungEx (CT-sim breathing) group. $^{\dagger}p<0.05$ vs. patient (free-breathing) group. Visual representation of lung gamma passing rates in the patient (b), 3D-BioLungEx (c), and ArcCHECK (d)

As illustrated in Fig. 9a, under the precise control of 3D-BioLungEx, the amplitude and cycle of patients' normal breathing in the CT simulation room were accurately replicated; this was called the CT-sim breathing pattern. Under this pattern, 3D-BioLungEx recorded the gamma passing rate of (93.61±5.00)%, significantly higher than that observed during free-breathing in the actual treatment ((90.25±3.64)%; $p<0.05$). This difference was attributed to the challenges patients face in replicating the CT simulation room breathing pattern during treatment; breathing inconsistencies negatively affected the gamma passing rates, reducing them below the anticipated 95% threshold.

In CS breathing, irregular rhythms with variable amplitudes produced the gamma passing rate of (87.71±3.09)%. The yawning pattern, characterized by expanded oral and pharyngeal regions, increased respiratory amplitude and decreased the gamma passing rate to (81.35±3.38)%. The coughing pattern involved intense thoracic movement, yielding the highest respiratory amplitude and further decreasing the gamma passing rate to (75.31±4.42)%. Across these abnormal patterns, the gamma passing rates gradually declined with increased respiratory amplitude.

To investigate the effects of respiratory amplitude and cycle on gamma passing rates, 3D-BioLungEx was used to adjust these parameters. Respiratory amplitude significantly affected gamma passing rates, while changes in cycle had no notable impact. With increasing amplitude, gamma passing rates declined. For example, with an amplitude variation of (A±20) mm, the passing rates dropped to below 80%. Conversely, with reduced amplitude variation, passing rates improved, especially when the amplitude decreased to (A±5) mm. In contrast, changes in respiratory cycle (within a range of (T±500) ms to (T±2000) ms) did not significantly affect the passing rates, which remained stable at 92%–94%. Notably, the gamma passing rate of ArcCHECK was (95.94±1.43)%, significantly higher than those obtained from the patient and 3D-BioLungEx.

Figure 9a presents an analysis of the impact of various respiratory patterns on global gamma passing rates. Figures 9b–9d provide a visual comparison of lung gamma passing rates for the patient, 3D-BioLungEx, and ArcCHECK, with purple regions indicating areas that failed to pass. Figure 9c focuses on lung gamma passing rates for porcine lung simulations driven by 3D-BioLungEx, divided into upper, middle, and lower sections. The upper section illustrates the effect of varying respiratory amplitude ((A–20) mm to (A+20) mm) while holding cycle constant, showing that increased amplitude correlates with larger non-passing areas and decreased gamma passing rates. The middle section highlights three abnormal respiratory patterns simulated by 3D-BioLungEx, with gamma passing rates progressively decreasing. The lower section examines the effect of respiratory cycle changes ((T–2000) ms to (T+2000) ms), with amplitude held constant, revealing no significant impact on lung gamma passing rates, as the purple non-passing regions remained stable.

4 Discussion

Our study demonstrates that respiratory motion significantly compromises radiotherapy dose delivery accuracy, with

gamma passing rates ranging from 78.54% for irregular breathing patterns to 95.86% under static conditions. The 3D-BioLungEx phantom successfully captured respiratory-induced dosimetric variations, showing measurable differences between CT-simulation breathing (93.47%) and actual treatment breathing (91.22%) conditions, with abnormal breathing patterns (Cheyne–Stokes, yawning, coughing) producing progressively worse dose conformity. These findings reveal a substantial 17.32% difference between optimal static conditions and the most challenging breathing pattern, highlighting the critical impact of respiratory motion on treatment accuracy.

These results align with and extend previous in vivo dose verification studies. Wu et al. [39] were the first to apply EPID-based 2D in vivo dose distribution verification to 30 cases of nasopharyngeal cancer, demonstrating its effectiveness in real-time dose monitoring during intensity-modulated radiation therapy (IMRT). Tan et al. [40] subsequently extended this approach to cervical cancer patients undergoing IMRT, further validating its reliability in tracking dynamic dose changes. However, Feng et al. [41] highlighted a common issue: the gamma passing rates for in vivo dose distribution verification were significantly lower than those for pretreatment rigid-body dose distribution verification, indicating dose deviations during actual treatment. Our findings corroborate these results, showing that the in vivo 3D dose distribution gamma passing rate for patients was lower than that for ArcCHECK. While ArcCHECK verifies dose distribution under stationary conditions, in vivo, respiratory motion and other physiological variations lead to fluctuations in dose distribution, resulting in a lower gamma passing rate. This underscores the urgent need to improve the accuracy of in vivo dose distribution verification.

Despite advances in in vivo dose distribution verification technology, its primary function has been retrospective, assessing the dose already delivered rather than serving as a preventive measure. Moreover, this technology is constrained by individual patient differences and physiological factors, particularly in the thoracic and abdominopelvic regions. These areas are more susceptible to physiological changes such as respiratory motion, gastrointestinal peristalsis, and bladder filling, which can lead to actual dose deviations from the planned dose [42–44]. In response, our study introduced an innovative method for biological in vivo 3D dose distribution verification to deepen our understanding of how respiratory motion specifically affects radiotherapy outcomes for lung cancer patients. Using the self-developed 3D-BioLungEx system, we successfully simulated the respiratory patterns of lung cancer patients and developed the IOSI-BLDose algorithm to precisely quantify dose discrepancies between actual and planned doses under various respiratory patterns.

Our results indicate that lung cancer patients' respiratory patterns during treatment often differ from those observed in the CT simulation room, leading to gamma passing rates slightly below expected levels. Accordingly, effective monitoring and control of respiratory motion during radiotherapy are pivotal for improving treatment outcomes [45].

In this study, the 3D-BioLungEx system was used to simulate various respiratory patterns and evaluate the impact on gamma passing rates. The results revealed that respiratory pattern consistency is essential for enhancing radiotherapy precision. When the 3D-BioLungEx accurately replicated the respiratory amplitude and cycle observed during simulation positioning in the CT simulation room, the gamma passing rates were close to 95%. Conversely, abnormal respiratory patterns significantly reduced the gamma passing rates. Variations in respiratory amplitude had a direct impact on gamma passing rates, while changes in respiratory cycle showed no notable effect.

In practice, the guidance curve is displayed on a visual monitor placed in front of the patient, overlaid with the real-time breathing waveform acquired via an external sensor (e.g., pressure belt or infrared marker system). Patients are instructed to visually align their breathing with the target curve. To quantify compliance, the system continuously calculates the correlation coefficient between the reference and actual breathing curves. When this coefficient exceeds a predefined threshold (e.g., $R>0.85$), breathing is considered compliant. Real-time auditory prompts may be given if deviation occurs, helping patients maintain synchrony.

The introduction of biological in vivo 3D dose distribution verification represents a significant transition from traditional static dose verification to dynamic, real-time validation. This approach not only simplifies workflows and reduces positioning errors by replacing conventional IMRT dose verification devices but also enables real-time monitoring of dose deviations during treatment, providing timely and reliable data to support clinical decision-making. While biological in vivo 3D dose verification has advanced dosimetric validation considerably, its current application is limited to controlling or guiding patient breathing, without achieving true beam compensation during radiotherapy. This limitation presents a clear direction for future research. Integrating this method with the patient's actual respiratory curve could enable real-time compensatory adjustments to the radiotherapy plan, achieving more precise adaptation to respiratory motion and further enhancing treatment accuracy and effectiveness [46].

5 Conclusions

In this study, we developed an innovative method for biological in vivo 3D dose distribution verification to investigate the impact of respiratory motion on lung cancer radiotherapy outcomes. The self-developed 3D-BioLungEx system

accurately simulated patient-specific respiratory patterns, while the IOSI-BLDose algorithm precisely quantified dose discrepancies between actual and planned doses. Our results showed that consistent respiratory patterns are essential for radiotherapy precision, with abnormal patterns reducing gamma passing rates. While respiratory amplitude variations significantly affected gamma passing rates, cycle changes had minimal impact. Our novel approach simplifies workflows, reduces positioning errors, and enables real-time monitoring of dose deviations. Future research should focus on integrating this method with the patient's actual respiratory curve for real-time radiotherapy plan adjustments, further enhancing treatment accuracy and effectiveness.

Acknowledgements This work is supported by the National Natural Science Foundation of China (No. 62371243), National Key Research and Development Program of China (No. 2025YFC2427600), the Jiangsu Provincial Key Research and Development Program Social Development Project (No. BE2022720), the Natural Science Foundation of Jiangsu Province (No. BK20231190), Jiangsu Provincial Medical Key Discipline Cultivation Unit of Oncology Therapeutics (Radiotherapy) (No. JSDW202237), Changzhou Social Development Program (Nos. CE20235063 and CJ20244020), and Postgraduate Research & Practice Innovation Program of Jiangsu Province (No. JX13614239).

Author contributions XYN conceived and designed the study, supervised and advanced the project. JRD provided clinical medical guidance and recommendations for this study. YTZ designed the device, developed the algorithm, and wrote the manuscript. HPZ participated in the improvement of the algorithm. KX and JWL participated in the improvement of the manuscript. KX and HPZ participated in the running of the experiment. LTS, QJH, and HW correlated the collected respiratory curves with both quantitative test results and qualitative subjective feelings. TL, LGG, and JWS provided ideas and needs of dose verification, as well as medical guidance for our work. All authors reviewed the manuscript.

Declarations

Conflict of interest The authors declare that they have no conflict of interest.

Ethical approval This study, including all the procedures involving animals that it entailed, was approved by the Ethics Committee of the Second People's Hospital of Changzhou (Approval No. [2024] KY115-01), and adhered to the 2013 revised Declaration of Helsinki (www.wma.net/en/30publications/10policies/b3/index.html). All participants gave informed consent (including consent for participation and consent for publication).

Data availability The data that support the findings of this study are available from the corresponding author upon reasonable request. The source code and the demonstration of 3D-BioLungEx and IOSI-BLDose are available at GitHub: https://github.com/NMUZYT/3D-BioLungEx-IOSI-BLDose.

References

1. Filho AM, Laversanne M, Ferlay J et al (2025) The GLOBOCAN 2022 cancer estimates: data sources, methods, and a snapshot of the cancer burden worldwide. Int J Cancer 156(7):1336–1346. https://doi.org/10.1002/ijc.35278
2. Vinod SK, Hau E (2020) Radiotherapy treatment for lung cancer: current status and future directions. Respirology 25(S2):61–71. https://doi.org/10.1111/resp.13870
3. Shao Y, Zhang XY, Wu G (2021) Prediction of three-dimensional radiotherapy optimal dose distributions for lung cancer patients with asymmetric network. IEEE J Biomed Health Inform 25(4): 1120–1127. https://doi.org/10.1109/JBHI.2020.3025712
4. Thomadsen B, Kapur A, Blankenship B et al (2024) AAPM task group report 288: recommendations for guiding radiotherapy event narratives. Med Phys 51(9):5858–5872. https://doi.org/10.1002/mp.17282
5. Gillmann C, Homolka N, Johnen W et al (2021) Technical Note: Adam PETer—an anthropomorphic, deformable and multimodality pelvis phantom with positron emission tomography extension for radiotherapy. Med Phys 48(4):1624–1632. https://doi.org/10.1002/mp.14597
6. Vásquez AC, Runz A, Echner G et al (2012) Comparison of two respiration monitoring systems for 4D imaging with a Siemens CT using a new dynamic breathing phantom. Phys Med Biol 57(9):N131–N143. https://doi.org/10.1088/0031-9155/57/9/N131
7. Kostiukhina N, Georg D, Rollet S et al (2017) Advanced Radiation DOSimetry phantom (ARDOS): a versatile breathing phantom for 4D radiation therapy and medical imaging. Phys Med Biol 62(20):8136–8153. https://doi.org/10.1088/1361-6560/aa86ea
8. Perrin RL, Zakova M, Peroni M et al (2017) An anthropomorphic breathing phantom of the thorax for testing new motion mitigation techniques for pencil beam scanning proton therapy. Phys Med Biol 62(6):2486. https://doi.org/10.1088/1361-6560/62/6/2486
9. Bondesson D, Meijers A, Janssens G et al (2022) Anthropomorphic lung phantom based validation of in-room proton therapy 4D-CBCT image correction for dose calculation. Z Med Phys 32(1):74–84. https://doi.org/10.1016/j.zemedi.2020.09.004
10. Rabe M, Paganelli C, Riboldi M et al (2021) Porcine lung phantom-based validation of estimated 4D-MRI using orthogonal cine imaging for low-field MR-Linacs. Phys Med Biol 66(5): 055006. https://doi.org/10.1088/1361-6560/abc937
11. Albers J, Wagner WL, Fiedler MO et al (2023) High resolution propagation-based lung imaging at clinically relevant X-ray dose levels. Sci Rep 13:4788. https://doi.org/10.1038/s41598-023-30870-y
12. Mann P, Witte M, Moser T et al (2017) 3D dosimetric validation of motion compensation concepts in radiotherapy using an anthropomorphic dynamic lung phantom. Phys Med Biol 62(2):573. https://doi.org/10.1088/1361-6560/aa51b1
13. Lin HL, Huang SM, Deng XW et al (2014) Comparison of 3D anatomical dose verification and 2D phantom dose verification of IMRT/VMAT treatments for nasopharyngeal carcinoma. Radiat Oncol 9:71. https://doi.org/10.1186/1748-717X-9-71
14. Tai YM, Heng VJ, Renaud MA et al (2023) Quality assurance for mixed electron–photon beam radiation therapy using treatment log files and MapCHECK. Med Phys 50(12):7996–8008. https://doi.org/10.1002/mp.16759
15. Sharma S, Chander S, Subramani V et al (2018) EP-1764: comparison of COMPASS beam modelling with Monaco using Elekta express QA beams. Radiother Oncol 127:S945–S946. https://doi.org/10.1016/S0167-8140(18)32073-5
16. Gorobets VA, De Vries JHW, Brand N et al (2024) 2621:

MR-compatible Octavius detector and phantom systems are suitable for plan QA in a 1.5 T MRI-linac. Radiother Oncol 194: S3355–S3358. https://doi.org/10.1016/S0167-8140(24)02795-6
17. Linsalata S, Satsi OA, Barca P et al (2024) 1222: EPID pretreatment PSQA with SunCheck PerFRACTION: a single center comparison with ArcCheck. Radiother Oncol 194:S3243–S3245. https://doi.org/10.1016/S0167-8140(24)01663-3
18. Biancardo SBN, Santurio GV (2021) PO-1587 feasibility of using the Scandidos Delta4 phantom+ for performing star-shot test on a MRIdian linac. Radiother Oncol 161:S1312–S1313. https://doi.org/10.1016/S0167-8140(21)08038-5
19. Cui GQ, Duan J, Yin FF (2025) Dose verification of 2 targets simultaneously for single-isocenter stereotactic radiation therapy and radiosurgery plans. Med Dosim 50(2):179–184. https://doi.org/10.1016/j.meddos.2024.12.006
20. Chang B, Tan T, Du JT et al (2024) Dispersive Fourier transform based dual-comb ranging. Nat Commun 15:4990. https://doi.org/10.1038/s41467-024-49438-z
21. Zhong YN, Tang JS, Li XY et al (2022) A memristor-based analogue reservoir computing system for real-time and power-efficient signal processing. Nat Electron 5(10):672–681. https://doi.org/10.1038/s41928-022-00838-3
22. Wang CD, Shao J, He YC et al (2024) Data-driven risk stratification and precision management of pulmonary nodules detected on chest computed tomography. Nat Med 30(11):3184–3195. https://doi.org/10.1038/s41591-024-03211-3
23. Chen H, Li DSY, Bar-Joseph Z (2023) SCS: cell segmentation for high-resolution spatial transcriptomics. Nat Meth 20(8): 1237–1243. https://doi.org/10.1038/s41592-023-01939-3
24. Wang YY, Yi CQ, Tian WX et al (2024) Free-space direct nanoscale 3D printing of metals and alloys enabled by two-photon decomposition and ultrafast optical trapping. Nat Mater 23(12): 1645–1653. https://doi.org/10.1038/s41563-024-01984-z
25. Grebenyuk S, Abdel Fattah AR, Kumar M et al (2023) Large-scale perfused tissues via synthetic 3D soft microfluidics. Nat Commun 14:193. https://doi.org/10.1038/s41467-022-35619-1
26. Biswas D, Lamperski A, Yang Y et al (2023) Mode switching in organisms for solving explore-versus-exploit problems. Nat Mach Intell 5(11):1285–1296. https://doi.org/10.1038/s42256-023-00745-y
27. Benam KH, Novak R, Ferrante TC et al (2020) Biomimetic smoking robot for in vitro inhalation exposure compatible with microfluidic organ chips. Nat Protoc 15(2):183–206. https://doi.org/10.1038/s41596-019-0230-y
28. Mills A, Aissaoui N, Maurel D et al (2022) A modular spring-loaded actuator for mechanical activation of membrane proteins. Nat Commun 13(1):3182. https://doi.org/10.1038/s41467-022-30745-2
29. Raisch M, Maftuhin W, Walter M et al (2021) A mechanochromic donor-acceptor torsional spring. Nat Commun 12:4243. https://doi.org/10.1038/s41467-021-24501-1
30. Liu XJ, Xie BH, Zhang D et al (2024) Unsupervised physics-informed deep learning for assessing pulmonary artery hemodynamics. Expert Syst Appl 257:125079. https://doi.org/10.1016/j.eswa.2024.125079
31. Xu ZJ, Cao LNY, Li CY et al (2023) Digital mapping of surface turbulence status and aerodynamic stall on wings of a flying aircraft. Nat Commun 14(1):2792. https://doi.org/10.1038/s41467-023-38486-6
32. Bian LH, Wang Z, Zhang YZ et al (2024) A broadband hyperspectral image sensor with high spatio-temporal resolution. Nature 635(8037):73–81. https://doi.org/10.1038/s41586-024-08109-1
33. Lyu QH, Neph R, Sheng K (2023) Tomographic detection of photon pairs produced from high-energy X-rays for the monitoring of radiotherapy dosing. Nat Biomed Eng 7(3):323–334. https://doi.org/10.1038/s41551-022-00953-8
34. Zhang J, Cheng ZB, Fan ZT et al (2022) A feasibility study for in vivo treatment verification of IMRT using Monte Carlo dose calculation and deep learning-based modelling of EPID detector response. Radiat Oncol 17(1):31. https://doi.org/10.1186/s13014-022-01999-3
35. Song H, Lee C, Baek J (2024) Full 3-D modulation transfer function estimation of tomosynthesis system using modified Richardson-Lucy deconvolution. Med Phys 51(4):2510–2525. https://doi.org/10.1002/mp.16843
36. Yu CY, Zong Y, Duan ML et al (2024) Adaptive ray tracing in freeform gradient-index media using an index directional derivative. Opt Lett 49(19):5375–5378. https://doi.org/10.1364/OL.530952
37. Sarkar D, Kang J, Wassie AT et al (2022) Revealing nanostructures in brain tissue via protein decrowding by iterative expansion microscopy. Nat Biomed Eng 6(9):1057–1073. https://doi.org/10.1038/s41551-022-00912-3
38. Sini C, Broggi S, Fiorino C et al (2015) Accuracy of dose calculation algorithms for static and rotational IMRT of lung cancer: a phantom study. Phys Med 31(4):382–390. https://doi.org/10.1016/j.ejmp.2015.02.013
39. Wu ZQ, Chen YH, Wang JZ et al (2020) A study of in vivo dosimetry verification based on EPID transit dose. China Oncol 30(9): 689–693. https://doi.org/10.19401/j.cnki.1007-3639.2020.09.008
40. Tan X, Luo H, Li S et al (2020) Preliminary results on in-vivo dose measurement of intensity-modulated radiotherapy for cervical cancer. Int J Radiat Oncol 108(3):e280. https://doi.org/10.1016/j.ijrobp.2020.07.671
41. Feng B, Yu L, Mo EW et al (2021) Evaluation of daily CT for EPID-based transit in vivo dosimetry. Front Oncol 11:782263. https://doi.org/10.3389/fonc.2021.782263
42. Stengl C, Muñoz ID, Arbes E et al (2024) Dosimetric study for breathing-induced motion effects in an abdominal pancreas phantom for carbon ion mini-beam radiotherapy. Med Phys 51(8): 5618–5631. https://doi.org/10.1002/mp.17077
43. Tominaga Y, Oita M, Miyata J et al (2024) Experimental validation of a 4D dynamic dose calculation model for proton pencil beam scanning without spot time stamp considering free-breathing motion. Med Phys 51(1):566–578. https://doi.org/10.1002/mp.16725
44. Murrer LHP, van der Werf L, Vaassen F et al (2024) 2600: surface guided RT for breast cancer: robustness of dose volume parameters for breathing movement. Radiother Oncol 194:S4095–S4098. https://doi.org/10.1016/S0167-8140(24)02776-2
45. Li GJ, Wang GY, Wei WG et al (2024) Cardiorespiratory motion characteristics and their dosimetric impact on cardiac stereotactic body radiotherapy. Med Phys 51(11):8551–8567. https://doi.org/10.1002/mp.17284
46. van Vlaenderen ARW, Nelissen KJ, Rijn JGM et al (2024) 388: CBCT-guided online adaptive radiotherapy in breast cancer patients–a prospective trial NL2021.0624. Radiother Oncol 194: S469–S473. https://doi.org/10.1016/S0167-8140(24)01023-5